Applied Thermal Engineering 246 (2024) 122928

Contents lists available at ScienceDirect

Applied Thermal Engineering

journal homepage: www.elsevier.com/locate/ate

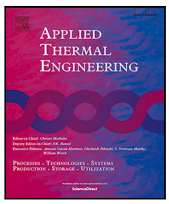

Research Paper

Transient mathematical modelling of a gas rotary furnace for melting slag

O. Crego [b], J.L. Ferrín [a,b,*], D. Gómez [a,b], L.J. Pérez-Pérez [c], P. Salgado [a,b]

[a] Departamento de Matemática Aplicada, Universidade de Santiago de Compostela, 15782 Santiago de Compostela, Spain
[b] Centro de Investigación y Tecnología Matemática de Galicia (CITMAga), 15782 Santiago de Compostela, Spain
[c] Departamento de Ingeniería Geológica y Minera, Universidad Politécnica de Madrid, 28003 Madrid, Spain

ARTICLE INFO

Keywords:
Numerical simulation
Combustion
Melting
Slag
Rotary kiln

ABSTRACT

A 2D transient mathematical model is proposed to analyse a gas rotary furnace intended for melting a CaO-SiO_2 slag, a crucial component to be used in the aluminothermic reduction for silicon production. The research, conducted in the framework of the EU SisAl Pilot project, aims to assess the feasibility of the industrial process of these furnaces and to recommend potential scale-up strategies. The mathematical model addresses two distinct but related issues. First, one problem is dedicated to the evaluation of the gas combustion characteristics, including the simulation of the natural gas flame as well as the heat transfer by convection and radiation. Secondly, the temperature data computed on the inner wall of the rotary kiln is used as a boundary condition to solve the problem of melting the solid material, thus determining the required melting time. The model is validated against experimental data for the melting of iron, the material currently used in the plant.

1. Introduction

High-purity silicon (Si), also known as silicon metal, is a material with extensive use in modern society, serving as an essential component of integrated circuit chips and transistors used in electronic devices or for the production of photovoltaic cells. Due to its importance for the European economy, it was added to the EU's list of critical raw materials in 2014 [1]. Despite silicon being the second most abundant element in the Earth's crust [2], it is rarely found as a pure element. Metallurgical grade silicon (>98% purity), which is the basis for all grades of silicon purity, is primarily manufactured by carbothermic reduction. While Submerged Arc Furnaces (SAF) are commonly employed for this purpose [3], other innovative techniques such as CO_2 laser beams [4] are also under development.

It is in this context that the SisAl project (www.sisal-pilot.eu) [5,6] was conceived. Funded by the EU's Horizon 2020 programme, this initiative aims to demonstrate a novel, patented process for the production of silicon alloys and high purity alumina from a more sustainable approach: the aluminothermic reduction of quartz using silicon dioxide and secondary raw materials such as scrap and aluminium dross to replace the carbon-based reductants currently used [7].

The SisAl process starts by heating a mixture of quartz and lime to a temperature of 1773 K, resulting in the formation of a suitable slag. Aluminium is then added, which reacts by reducing the quartz:

$$SiO_2(CaO - SiO_2 \text{ slag}) + \frac{4}{3}Al \rightarrow Si + \frac{2}{3}Al_2O_3(CaO - Al_2O_3 \text{ slag})$$

Finally, the resulting calcium aluminate slag can be further processed to produce high-purity aluminium [7].

Energy requirements are reduced due to the lower melting point of the CaO–SiO_2 slag compared to quartz and the exothermic nature of the aluminothermic reduction process. Thus, the SisAl approach represents an alternative to the traditional SAF process, allowing lower energy consumption and avoiding the direct CO_2 emissions associated with conventional carbothermic reduction. It also fosters industrial symbiosis by connecting the aluminium and silicon industries, leading to reduced material waste and improved waste recovery, thereby supporting the principles of the circular economy.

The project includes laboratory and pilot scale experimentation using different types of furnaces, such as induction and rotary kilns. In addition to experimental investigations, process optimization also relies on numerical modelling techniques. In this paper, we focus on the first stage of the process, the preparation of the SiO_2–CaO slag in a rotary kiln. Rotary kilns are a type of heat exchanger widely used in various industries for many processes, such as drying, heating and reduction of materials. They consist of a steel cylinder lined with refractory material and fitted with a rotating motor to create a rotary motion [8].

The design of melting furnaces has traditionally relied on semi-empirical methods due to the intricate nature of the involved processes. However, the challenging conditions within these furnaces pose obstacles to conducting experimental measurements. Therefore, mathematical modelling and numerical simulation have become an attractive alternative to aid their design and scale-up [9].

* Corresponding author at: Departamento de Matemática Aplicada, Universidade de Santiago de Compostela, 15782 Santiago de Compostela, Spain.
E-mail addresses: oscar.crego@usc.es (O. Crego), joseluis.ferrin@usc.es (J.L. Ferrín), mdolores.gomez@usc.es (D. Gómez), luisjavier.perez@upm.es (L.J. Pérez-Pérez), mpilar.salgado@usc.es (P. Salgado).

https://doi.org/10.1016/j.applthermaleng.2024.122928
Received 17 November 2023; Received in revised form 16 February 2024; Accepted 10 March 2024
Available online 12 March 2024

Nomenclature

Greek symbols

α	Liquid fraction [−]
β	Thermal expansion coefficient [1/K]
ϵ	Dissipation rate [J/(kg s)]
ε	Emissivity [−]
Γ	Boundary of Ω
μ	Dynamic viscosity [Pa s]
μ_T	Eddy viscosity [Pa s]
ρ	Density [kg/m^3]
Σ	Interface between subdomains
σ_s	Scattering coefficient [m^{-1}]
$\boldsymbol{\tau}^R$	Reynolds stress tensor [Pa]
Ω	Computational domain

Latin symbols

A_m	Mushy zone parameter [−]
a	Absorption coefficient [m^{-1}]
$\mathbf{b}$	Density of body force [N/m^3]
c_p	Specific heat [J/(kg K)]
$\mathbf{D}(\mathbf{v})$	Symmetric part of the velocity gradient [1/s]
D_m	Mass diffusion coefficient [m^2/s]
E	Total energy [J/kg]
$\mathbf{g}$	Gravitational acceleration [m/s^2]
H	Specific enthalpy [J/kg]
h	Heat transfer coefficient [W/(m^2 K)]
$\mathbf{I}$	Identity tensor
I	Radiation intensity [W/sr^{-1}]
I_b	Black-body radiation intensity [W/sr^{-1}]
K	Turbulent kinetic energy [m^2/s^2]
k	Thermal conductivity [W/(m K)]
k_{eff}	Effective thermal conductivity [W/(m K)]
L	Latent heat of fusion [J/kg]
$\dot{m}$	Mass flow rate [kg/s]
N	Number of involved species
$\mathbf{n}$	Outward-pointing unit normal vector [−]
p	Pressure [Pa]
t	Time [s]
t_{end}	Final time value [s]
T	Temperature [K]
T_{ext}	Ambient temperature [K]
$\mathbf{v}$	Velocity [m/s]
$\mathbf{x}$	Vector of spatial coordinates [m]

Subscripts

$_B$	Furnace bed
$_G$	Gas
$_{liq}$	Liquidus
$_{sol}$	Solidus
$_R$	Refractory

Acronyms

CFD	Computational Fluid Dynamics
EDM	Eddy Dissipation Model
RKE	Realizable $K-\epsilon$ model
RTE	Radiative Transfer Equation
SAF	Submerged Arc Furnace
WSGGM	Weighted Sum of Gray Gases Model

Rotary furnaces play a pivotal role in the cement industry, facilitating the production of cement clinker, an intermediate material crucial for cement manufacturing. Cement clinker is created through the sintering process of a blend of milled limestone and clay. Hence, there exists a significant amount of research dedicated to modelling and numerically simulating rotary furnaces, considering their specific characteristics and operational complexities. Given that cement kilns typically measure approximately 50 m in length and have a diameter of around 3 m, the majority of existing literature considers the furnace load (usually known as the bed) as a one-dimensional domain [10], while the gas (known as the freeboard region) is often modelled using 3D CFD models [11]. Some authors have considered detailed models for combustion, often focusing on coal (see e.g. [12]), and occasionally exploring alternative fuels like refuse-derived fuel [13]. In [14], the characteristics of a typical methane flame inside a rotary kiln were studied using an axisymmetric CFD model. The study investigated the impact of various parameters, including the swirl number.

In cement kilns, partial melting of the furnace bed is usually modelled with simplified approaches, such as assuming that the melt fraction is proportional to the bed temperature [15]. Drum rotation, typically around 3–4 rpm, is crucial for effectively mixing the furnace charge. Additionally, since the raw mix is milled before entering the furnace, some researchers have addressed the granular flow of solids in the kiln [16,17].

It should be noted that the application to the cement industry is significantly different from that of the SisAl slag. Specifically, while some complexities regarding chemical reactions are not relevant in the setting proposed in this paper, the melting of the furnace load is complete, as opposed to the case in cement kilns, where only partial melting is achieved. Therefore, more detailed melting models are required. To the best of the author's knowledge, the literature regarding this specific application is rather scarce.

In [18], a CFD model capable of predicting the melting rate of aluminium scrap and the energy distribution inside the furnace was proposed. The furnace load is considered as a static liquid, neglecting any rotation-induced motion and buoyancy. Melting is treated considering a Population Balance Model. In [19], the behaviour of a rotary kiln used to reduce iron ore to metallic iron in the sponge iron industry is modelled. A 2D longitudinal model is considered to account for the temperature profile in the bed and gas along the length of the kiln. Recently, a novel process concept has been developed for the recycling of solid residues and the production of secondary aluminium using a solar heated rotary kiln [20]. A review dealing with this specific application is available in [21].

In the present work, a 2D transient mathematical model of a gas rotary furnace for melting a CaO–SiO_2 slag suitable for the SisAl process is proposed. The aim is to evaluate the viability of the industrial process using this type of furnace and to suggest possible scale-up solutions. Since the modelled furnace is currently used to melt grey cast iron EN-GJL-250, the model is validated considering this specific material instead of the SisAl slag. This kind of iron is also commonly known as *gg25*.

The paper is organized as follows. In Section 2, the industrial furnace modelled in this work is described, as well as the typical operating procedure and the material properties considered along the paper. In Section 3, the complete mathematical model is presented. In Section 4, the computational grid and the methodology used to compute the solution are described. The numerical results obtained for the validation problem and the slag melting problem are discussed. Lastly, in Section 5, some concluding remarks are made.

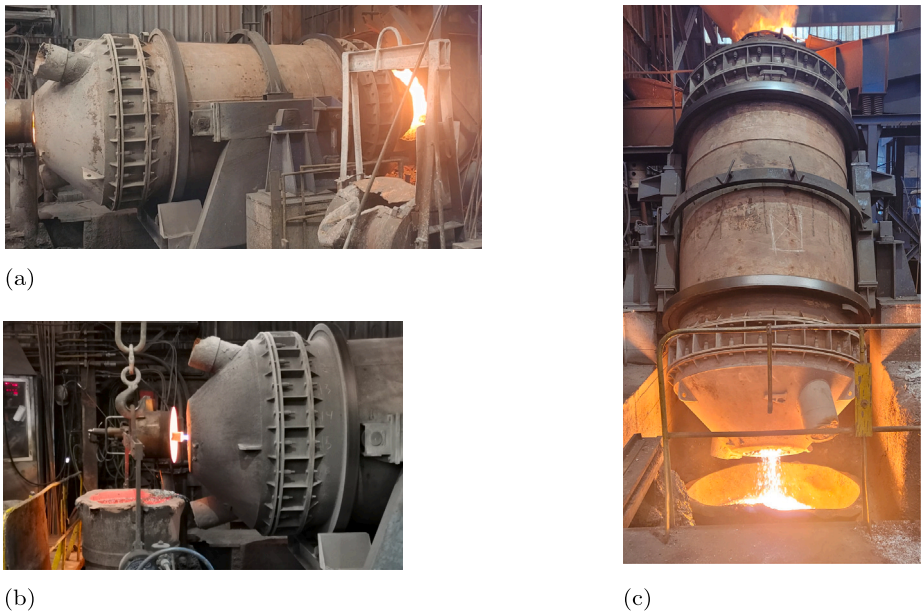

Fig. 1. Rotary furnace during normal operation at Fundiciones Rey facilities: (a) lateral view of the furnace, (b) flame with burner lid partially open, (c) furnace tilted for molten material drainage.

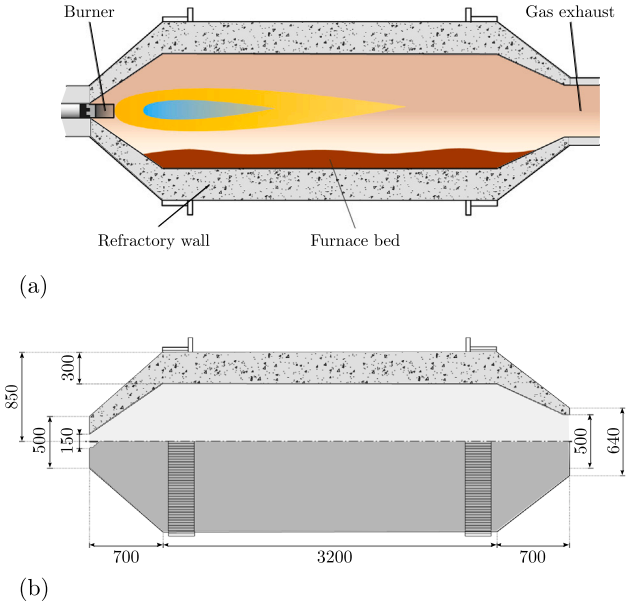

Fig. 2. Longitudinal cross-section of the gas rotary furnace: (a) schematic diagram, (b) drawing with dimensions (in mm).

Fig. 3. Pieces of iron used to load the rotary furnace.

2. Problem description

The furnace that is modelled in this work is a 4.6 m-long industrial rotary gas furnace available at the facilities of Fundiciones Rey in Spain. It has a maximum radius of 0.85 m and is shown in Fig. 1 during various operation stages. The furnace is made of a cylindrical steel vessel lined with a 300 mm thick refractory coating, which rolls around its axial direction following two turned rings that act as guides. The rotation of the cylinder is achieved by means of an electrically driven motor. This motion enhances the mixing of the partially molten materials and homogenizes the temperature inside the furnace.

As shown in Fig. 1, the furnace can be tilted to facilitate the loading of solid material and to drain the molten metal. Prior to the heating process, the furnace is returned to a horizontal position and connected to an exhaust gas collection hood, which remains open throughout the operation. On the opposite side, the furnace is closed with a lid that includes an oxy-fuel burner in its centre. The burner injects natural gas and oxygen generating an intense flame, as illustrated in the schematic diagram shown in Fig. 2. The process concludes upon complete melting of the material, at which point it is discharged through the burner side following tilting of the furnace.

To validate the model, and since the furnace is currently being used for iron melting, the typical operation cycle in the industrial facility is replicated in the mathematical model. During a normal day, three different casts are carried out after a preheating process with an empty furnace. The iron used to feed the furnace is depicted in Fig. 3.

2.1. Material properties

To model the properties of the various materials involved in the furnace operation, we use temperature-dependent data when available, either supplied by Fundiciones Rey or extracted from the literature. The constant values or the corresponding functions are summarized in Table 1. For the temperature-dependent functions, except for air density and iron viscosity, we employ piecewise linear interpolation of table values. In particular, in Fig. 4(a), the functions used for iron properties ($k_{iron}(T)$ and $c_{p,iron}(T)$) are depicted, according to the values extracted from [22]. In Fig. 4(b), the functions considered for refractory properties are shown. Figs. 5(a) and 5(b) illustrate the functions

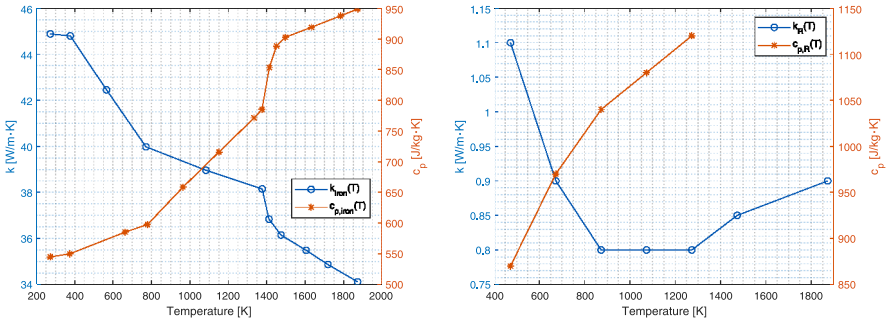

(a) $k_{iron}(T)$ and $c_{p,iron}(T)$. Source: [22]. (b) $k_R(T)$ and $c_{p,R}(T)$.

Fig. 4. Temperature-dependent properties of iron (left) and refractory (right).

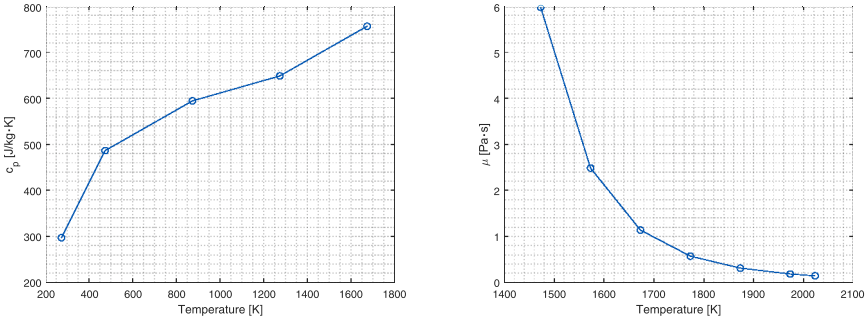

(a) $c_{p,slag}(T)$. (b) $\mu_{slag}(T)$.

Fig. 5. Temperature-dependent properties of slag.

Table 1
Physical properties of air, refractory, slag and EN-GJL-250 iron in the simulation.

	ρ [kg/m^3]	k [W/(m K)]	c_p [J/(kg K)]	μ [Pa s]
Gas	$\rho_G(\mathbf{Y},T)$	0.0454	$c_{p,G}(\mathbf{Y},T)$	1.72e−5
Refractory	2300	$k_R(T)$	$c_{p,R}(T)$	–
Slag	2591.635	1.0	$c_{p,slag}(T)$	$\mu_{slag}(T)$
Iron	7076.6	$k_{iron}(T)$	$c_{p,iron}(T)$	$\mu_{iron}(T)$

Table 2
Thermal expansion coefficient (β), latent heat (L), solidus (T_{sol}) and liquidus (T_{liq}) temperature of EN-GJL-250 iron and slag. A suitable temperature range for the phase change of both materials has been considered.

	Iron	Slag
β [K^{-1}]	4.6707e−5	1.0e−4
L [J/kg]	327 942	740 855.4
T_{sol} [K]	1330.15	1673.15
T_{liq} [K]	1517.15	1673.15

corresponding to the slag specific heat, $c_{p,slag}(T)$, and viscosity, $\mu_{slag}(T)$. The viscosity of iron is assumed to satisfy the following polynomial:

$$\mu_{iron}(T) = 1.571497 \cdot 10^{-2} - 8.315068 \cdot 10^{-6} T. \quad (1)$$

The values considered for the melting-related quantities, such as liquidus and solidus temperatures, as well as the latent heat of fusion and the thermal expansion coefficient of slag and iron, are gathered in Table 2. In the slag, instead of considering a single temperature value for fusion, a range $T_{sol} = 1668.15$ K, $T_{liq} = 1678.15$ K is selected due to convergence difficulties with the solid melting model (see Section 3.2). Lastly, the air in the gas combustion problem is modelled using the low Mach number approximation, i.e., its density depends on the temperature and the mass fraction of all the involved species in the combustion problem. With $\mathbf{Y}$, we denote the vector containing all species mass fractions, i.e. $\mathbf{Y} = (Y_1, \dots, Y_5)$, where Y_i is the mass fraction of the ith species (see Section 3.1). Also, the gas specific heat, $c_{p,G}$, depends on the mass fractions of all involved species and the temperature.

3. Mathematical model

The modelling of the heat transfer within rotary furnaces involves conduction, convection and radiation. The heat source is a natural gas flame, which generates strong currents in the air region, enhancing the convection heat transfer towards the initially solid furnace bed. Furthermore, the large temperature gradients in the solid induce liquid motion as the solid melts, greatly enhanced by the rotary furnace turning motion.

This work aims to address the simulation of complete furnace casts under various conditions, considering both the material currently used in the industrial setting and a slag suitable for the SisAl process. Due to the extended duration required in the plant to melt a typical load of iron (approximately 3500 kg), the numerical solution of a fully coupled transient 3D CFD model incorporating all the associated physical phenomena is not computationally feasible.

To simplify the problem, we adopt a two-step approach. In the first step, we focus on a detailed assessment of gas combustion. Utilizing a 2D longitudinal cut of the furnace and an axisymmetric model, we simulate the natural gas flame and study heat transfer through convection and radiation. For this stage, we assume an empty furnace. In the second step, we address the solid melting process. To mitigate the computational complexity, we consider a transversal 2D cross-section of the furnace as the computational domain. Furthermore, we assume that the presence of the load within the furnace would not significantly alter the surface temperature due to combustion. Thus, the averaged temperature on the boundary, computed in the previous gas combustion simulation, is utilized as input data for this step, whose main objective is to determine the time required for the load to melt.

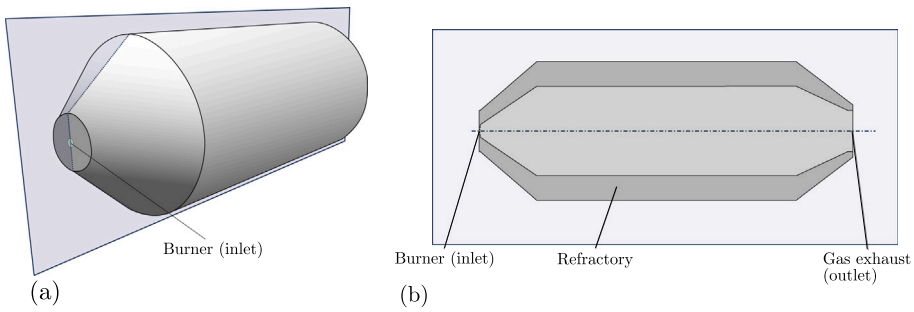

Fig. 6. Scheme of the rotary furnace for the gas combustion problem: (a) 3D view, (b) longitudinal cross-section.

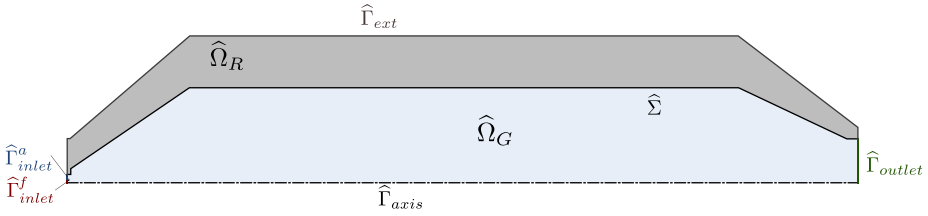

Fig. 7. Computational domain and boundaries in the gas combustion problem.

By dividing the problem into these two distinct steps, we can efficiently simulate complete furnace casts under various conditions while capturing the critical aspects of gas combustion and solid melting.

3.1. Gas combustion problem

In the gas combustion problem, a 2D axisymmetric model defined in a longitudinal cross-section of the furnace depicted in Fig. 6 is solved. The oxy-fuel burner has an annular configuration, with a circular fuel nozzle surrounded by an annulus which injects air into the furnace. It is attached to a refractory lid that closes one side of the rotary kiln during operation. The fuel nozzle has a diameter of 10 mm whereas the air nozzle has an inner diameter of 15 mm and an outer diameter of 40 mm. The fuel (natural gas) is modelled as pure methane. We assume a methane mass flow rate of 0.0298 kg/s and an air injection rate of 0.512 kg/s.

The computational domain and its corresponding subdomains and boundaries are depicted in Fig. 7. The complete domain, denoted as $\widehat{\Omega}$, is split into two subdomains: one corresponding to the gas, $\widehat{\Omega}_G$, and another representing the solid refractory surrounding the gas, denoted as $\widehat{\Omega}_R$.

3.1.1. Model equations

To model the methane combustion within the rotary kiln, we consider a CFD model involving the Navier–Stokes equations, the energy conservation equation and species transport equations. Specifically, the mass and momentum conservation equations are solved in $\widehat{\Omega}_G$:

$$\frac{\partial \rho}{\partial t} + \operatorname{div}(\rho \mathbf{v}) = 0, \tag{2}$$

$$\frac{\partial}{\partial t}(\rho \mathbf{v}) + \operatorname{div}(\rho \mathbf{v} \otimes \mathbf{v}) = -\operatorname{grad}(p) - \operatorname{div}\left((\mu + \mu_T)\left[2\mathbf{D}(\mathbf{v}) - \frac{2}{3}\operatorname{div}(\mathbf{v})\mathbf{I}\right] - \frac{2}{3}\rho K \mathbf{I} \right), \tag{3}$$

where $\mathbf{v}$ is the fluid velocity, p denotes the pressure and μ_T is the turbulent viscosity. Furthermore, $\mathbf{D}(\mathbf{v})$ denotes the symmetric part of the velocity gradient, i.e., $\mathbf{D}(\mathbf{v}) = (\operatorname{grad}(\mathbf{v}) + \operatorname{grad}(\mathbf{v})^T)/2$. Lastly, $\mathbf{I}$ is the identity tensor.

The density, ρ, and viscosity μ in (2)–(3) are taken as those corresponding to gas in Table 1. Therefore, gas density is variable and depends on the temperature and the species mass fractions. Specifically, we recall that the gas is modelled as a mixture following the low Mach number approximation (*incompressible ideal-gas* law in ANSYS Fluent [23]).

Since the flow is turbulent with variable density, the previous equations are interpreted as the Favre-averaged Navier–Stokes equations, i.e., the velocity represents a mass-averaged value and the pressure is the standard time-averaged value (see [24]). To account for turbulence in the flow, the Realizable $K-\epsilon$ model (RKE) is used, which is a two equation RANS turbulence model widely used in similar industrial applications (see e.g. [14,25]). It solves two additional conservation equations for the turbulent kinetic energy, K, and the dissipation rate, ϵ:

$$\frac{\partial}{\partial t}(\rho K) + \operatorname{div}(\rho K \mathbf{v}) = \operatorname{div}\left(\left(\mu + \frac{\mu_T}{\sigma_k} \right) \operatorname{grad} K \right) + G_K + G_b - \rho\epsilon - Y_M, \tag{4}$$

$$\frac{\partial}{\partial t}(\rho \epsilon) + \operatorname{div}(\rho \epsilon \mathbf{v}) = \operatorname{div}\left(\left(\mu + \frac{\mu_T}{\sigma_\epsilon} \right) \operatorname{grad}\epsilon \right) + \rho C_1 S \epsilon - \rho C_2 \frac{\epsilon^2}{K + \sqrt{\nu\epsilon}} + C_{1\epsilon}\frac{\epsilon}{K} C_{3\epsilon} G_b. \tag{5}$$

The turbulent viscosity, μ_T, is computed as follows

$$\mu_T = \rho C_\mu(K, \epsilon)\frac{K^2}{\epsilon}. \tag{6}$$

In the previous equations, the source term G_K represents the production of turbulent kinetic energy, G_b is the production of kinetic energy due to buoyancy, and Y_M models contributions to the dissipation rate due to the fluctuating dilatation in compressible turbulence. In addition, S is the strain rate magnitude, $C_{1\epsilon}$ and C_2 are model constants, while σ_K and σ_ϵ are the turbulent Prandtl numbers for K and ϵ, respectively. The precise definitions of the various source terms and constants involved in (4)–(6) are omitted for the sake of brevity. For their specific definition in the RKE model, we refer the interested reader to [23].

Furthermore, the energy conservation equation is solved in $\widehat{\Omega}_G$:

$$\frac{\partial}{\partial t}(\rho H) + \operatorname{div}(\rho \mathbf{v} H) = \operatorname{div}\left(k_{eff} \operatorname{grad} T - \sum_{i=1}^{N} H_i \mathbf{J}_i \right) + S_h, \tag{7}$$

where N is the total number of involved chemical species and H is the specific enthalpy, computed as

$$H = \sum_{i=1}^{N} Y_i H_i + \frac{p}{\rho},$$

being Y_i and H_i the mass fraction and enthalpy of the ith chemical species (see Section 3.1.2), respectively. The enthalpy of the chemical species only includes changes due to specific heat, i.e.:

$$H_i(T) = \int_{T_{ref}}^{T} c_{p,i}(s)ds, \tag{8}$$

with $c_{p,i}$ being the specific heat of the ith species and T_{ref} a reference temperature.

Moreover, in (7), $\mathbf{J}_i$ is the ith species diffusion flux, discussed in Section 3.1.2, and k_{eff} denotes the effective thermal conductivity, obtained as

$$k_{eff} = k + \frac{c_p \mu_T}{Pr_T}, \tag{9}$$

being k the thermal conductivity of the gas and Pr_T the turbulent Prandtl number, considered as $Pr_T = 0.85$. Finally, in (7), the source term S_h includes contributions due to the chemical reactions and the radiative heat transfer.

The solid subdomain is defined by the refractory wall of the rotary kiln and denoted as $\widehat{\Omega}_R$ (see Fig. 6). In $\widehat{\Omega}_R$, the heat conduction is modelled by the classical heat equation:

$$\rho c_p \frac{\partial T}{\partial t} - \mathrm{div}(k\,\mathrm{grad}\,T) = 0, \tag{10}$$

where the density, ρ, specific heat, c_p and thermal conductivity, k, correspond to those values for the refractory in Table 1.

Note that since the model is 2D axisymmetric, all equations concerning the model for the gas combustion problem are rewritten in cylindrical coordinates assuming symmetry in the azimuthal direction.

3.1.2. Combustion modelling

As mentioned previously, natural gas is modelled as pure methane. Its combustion is described with a one-step reaction mechanism

$$CH_4 + 2O_2 \rightarrow CO_2 + 2H_2O. \tag{11}$$

Hence, conservation equations for the mass fractions of each of the previous species, as well as N_2, are considered:

$$\frac{\partial \rho Y_i}{\partial t} + \mathrm{div}(\rho \mathbf{v} Y_i) = -\mathrm{div}(\mathbf{J}_i) + R_i, \tag{12}$$

where R_i is the net rate of production of the ith species ($i = 1, \ldots, 5$) due to the reaction mechanism. Moreover, $\mathbf{J}_i$ is the diffusion flux of the species, modelled considering that

$$\mathbf{J}_i = -\left(\rho D_m + \frac{\mu_T}{Sc_T}\right)\mathrm{grad} Y_i, \tag{13}$$

where Sc_T is the turbulent Schmidt number, considered as $Sc_T = 0.7$, and $D_m = 2.88e-5$ m^2/s is the mass diffusion coefficient.

To model the combustion process, the Eddy Dissipation Model (EDM) is used [26]. It considers the rate of dissipation of eddies to determine the reaction rates, under the assumption that chemical kinetic rates are considerably faster than rates of turbulent mixing [27]. Hence, instantaneous burn upon mixing is assumed. For more details on the specific implementation of this model in the software package used for the numerical simulation, we refer to [23].

3.1.3. Radiation model

To model the radiative heat transfer in the furnace, the Discrete Ordinates (DO) model is used, which is suitable for participating media that is not optically thick enough to justify approximations such as the P1 model (see, for instance, [28]). The model solves the radiative transfer equation (RTE):

$$\mathrm{div}_{\mathbf{x}}(I(\mathbf{x},\mathbf{s})) + (a+\sigma_s)I(\mathbf{x},\mathbf{s}) = aI_b + \frac{\sigma_s}{4\pi}\int_{S^2} \phi(\hat{\mathbf{s}},\mathbf{s})I(\mathbf{x},\hat{\mathbf{s}})dA_{\hat{\mathbf{s}}}, \tag{14}$$

where I denotes the radiation intensity, which depends on the position, $\mathbf{x}$, and the direction in the unit sphere S^2, denoted as $\mathbf{s}$. Furthermore, $dA_{\hat{\mathbf{s}}}$ is the surface area element in the sphere or, equivalently, the solid angle. The scattering coefficient, denoted as σ_s, is considered in this paper as a constant with value $\sigma_s = 0.01$ m^{-1} and ϕ denotes the scattering phase function, which is assumed isotropic. Lastly, I_b is the black-body radiation intensity (see [28]) and the absorption coefficient, a, depends on the temperature and the species mass fractions. It is calculated according to the Weighted Sum of Gray Gases model (WSGGM) (see [23,29]), which assumes that it depends on the temperature and mass fractions of the species involved.

To discretize (14), different directions in the total solid angle are considered, replacing the integrals over the directions using numerical quadrature (see [30]). Note that radiation is only solved in the gas subdomain $\widehat{\Omega}_G$, as the solid is assumed opaque.

3.1.4. Boundary and initial conditions

The boundary of the computational domain $\widehat{\Omega}$ is decomposed as depicted in Fig. 7. On the exterior boundary, denoted as $\widehat{\Gamma}_{ext}$, convective heat exchange with the air surrounding the rotary kiln is imposed:

$$-k\frac{\partial T}{\partial \mathbf{n}} = h(T)(T - T_{ext}), \tag{15}$$

where the value of the ambient temperature is $T_{ext} = 293.15$ K and the heat transfer coefficient, h, follows the subsequent temperature-dependent function:

$$h(T) = 0.01412\left(0.3221(6.757\cdot 10^8 T - 1.98\cdot 10^{11})^{1/6} + 0.6\right)^2, \tag{16}$$

which was obtained from standard heat transfer correlations for natural convection around a cylinder (see [31]).

On $\widehat{\Sigma}$, which corresponds to the interface between the solid refractory and the gas within the rotary furnace, we set a no-slip condition ($\mathbf{v} = \mathbf{0}$). This condition is set considering the dimensionless wall distance by using the *enhanced wall treatment* in ANSYS Fluent (see [23]). Furthermore, continuity of heat flux and temperature is set.

Moreover, on the fuel inlet, denoted as $\widehat{\Gamma}^f_{inlet}$, the mass flow rate is set, considering $\dot{m} = 0.02982$ kg/s, a turbulent intensity of 5% and a hydraulic diameter of 0.01 m, which are used to set the values of K and ϵ. The temperature is $T = 293.15$ K, and the mass fraction of CH_4 is one. On the other hand, in the air inlet $\widehat{\Gamma}^a_{inlet}$, a mass flow rate $\dot{m} = 0.5121$ kg/s, a turbulent intensity of 5% and a hydraulic diameter of 0.04 m are set, also considering $T = 293.15$ K. Lastly, the mass species fractions are set to 0.232 of O_2 and 0.768 of N_2.

On the symmetry axis $\widehat{\Gamma}_{axis}$, the normal derivatives of all variables are null, whereas on the outlet $\widehat{\Gamma}_{outlet}$ the *pressure-outlet* boundary condition is specified with a pressure value $p = 0$.

The emissivity of the walls surrounding the gas subdomain ($\widehat{\Sigma}$) is set to $\varepsilon = 0.85$, whereas the emissivity of the fictitious boundaries ($\widehat{\Gamma}^f_{inlet}$, $\widehat{\Gamma}^a_{inlet}$ and $\widehat{\Gamma}_{outlet}$) is $\varepsilon = 1$, with a fixed boundary temperature $T = 293.15$ K.

As the initial condition, we set that the velocity is $\mathbf{v} = 0$ m/s and the temperature $T = 293.15$ K. The turbulent variables are set as $K = 0$ m^2/s^2 and $\epsilon = 1$ m^2/s^3, whereas the initial species mass fractions are 0.232 for O_2 and 0.768 for N_2.

3.2. Solid melting problem

In the solid melting problem, the model is defined in the 2D cross-section depicted in Fig. 8, which considers a transversal cut of the rotary furnace. As mentioned previously, the goal is to assess the time required to melt a set amount of material. Physically, the system within the furnace is a multiphase fluid, comprising both the furnace bed, where a melting process takes place, and the region occupied by the gas, inside a domain with a moving part. Due to the significant computational requirements associated with the direct solution of the real problem, several simplifications are made.

Firstly, the phase corresponding to the gaseous mixture – where methane combustion takes place – is excluded from consideration. Instead, its influence is approximated by a prescribed temperature

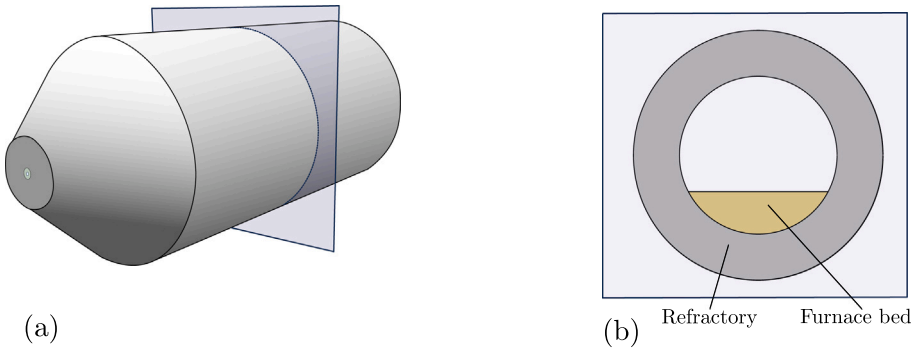

Fig. 8. Transversal cross-section of the rotary furnace for the solid melting problem: (a) 3D view, (b) computational domain.

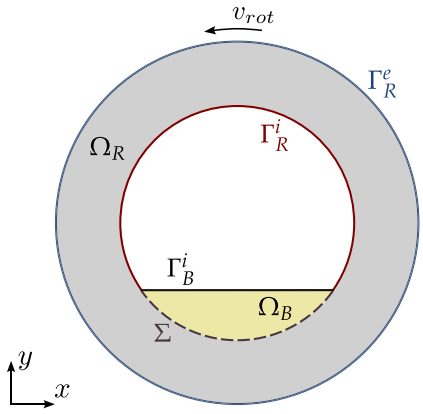

Fig. 9. Computational domain and boundaries of the solid melting problem seen from the burner.

boundary condition. It is also assumed that the region initially occupied by the solid phase (iron or slag) retains its predetermined shape and position throughout the simulation. Since the relative density variations of iron and slag during the heating and melting process are small, the volume expansion due to the melting is neglected. Despite not accounting for volume expansion, the model still incorporates buoyancy forces due to density changes in the molten or partially molten material, as they may significantly enhance mixing in the furnace bed.

Lastly, it should be noted that the solid material consists of pieces. The model does not take into account the spaces between them. For iron, these pieces are relatively large, as shown in Fig. 3.

A CFD model solving similar equations to those presented in Section 3.1.1 is considered. As mentioned above, the gas subdomain is not included in this stage and, instead, the computed temperature over time as the solution to the gas combustion problem is used as a boundary condition to account for the heat provided by the natural gas combustion.

The computational domain for this problem, denoted as Ω, as well as its subdomains and boundaries, are depicted in Fig. 9. The view of the corresponding transversal section is displayed as it would be seen from the burner side, resulting in a counter-clockwise rotation of the kiln. The domain is split into a subdomain corresponding to the furnace load, Ω_B, and a subdomain corresponding to the solid refractory, denoted as Ω_R.

The mathematical model accounts for the conjugate heat transfer between the refractory and the furnace load occupying Ω_B. The load is assumed to be either iron or slag, as discussed in Section 2, initially in solid state. To model the melting, a standard enthalpy-porosity technique discussed below is used. In the molten materials, we account for buoyancy due to density difference and the enhanced mixing due to the furnace rotation by solving the Navier–Stokes equations, considering the Boussinesq model for buoyancy and suitable boundary conditions.

3.2.1. Melting submodel

To model the melting of either iron or slag, we utilize a fixed-grid, enthalpy-porosity formulation proposed in [32]. This formulation has been widely adopted in similar applications involving the melting of different materials in furnaces (see e.g. [9]). The technique does not explicitly track the molten interface. Instead, a variable representing the liquid fraction, α, is introduced, which varies from zero (solid phase) to 1 (liquid phase). Intermediate values indicate the presence of an artificial mushy region, assumed to behave as a porous medium. The liquid fraction indicates the permeability of the mushy zone, and appropriate source terms are defined to ensure that the flow velocity reduces with decreasing liquid fraction, reaching zero when the mush becomes completely solid. Specifically, the liquid fraction α is computed at each iteration as

$$\alpha = \begin{cases} 0, & \text{if } T < T_{sol}, \\ \dfrac{T - T_{sol}}{T_{liq} - T_{sol}}, & \text{if } T_{sol} \le T \le T_{liq}, \\ 1, & \text{if } T > T_{liq}. \end{cases}$$

The model reformulates the energy equation (7), adjusting the definition of enthalpy to include the latent heat due to the phase change, L:

$$H = \int_{T_{ref}}^{T} c_p(s)ds + \alpha L. \tag{17}$$

The liquid–solid mushy zone, where $\alpha \in (0, 1)$, as indicated above, is treated as a porous material with porosity equal to the liquid fraction. To model the flow in this porous region, a source term is added. Its value increases from zero when $\alpha = 1$, allowing free motion in the liquid phase, to a value which ensures that the source term dominates the transient, convective, and diffusive terms in the conservation equations, effectively forcing the velocity to take near zero values [32]. In particular, the subsequent source term is added to the momentum conservation equation (3) and the turbulence variables Eqs. (4)–(5):

$$S = \frac{(1-\alpha)^2}{(\alpha^3 + \gamma)} A_m \varphi, \tag{18}$$

where φ is the variable involved in each equation (either $\mathbf{v}$, K or ϵ). This source term is obtained as a modified form of the Carman–Kozeny equation, derived from the Darcy's law for fluid flow in porous media.

In (18), the parameter $\gamma = 0.001$ is introduced to avoid division by zero and the so-called mushy zone constant, A_m, measures the amplitude of the damping due to the partially solidified region, i.e., how fast the fluid velocity approaches zero as it solidifies. Usually, A_m is selected with values between $1e4$ and $1e8$, depending on the specific features of the problem [23,32]. Note that the effect that the value of the mushy zone constant has on the numerical predictions is significant, as shown in [33], where simulations were conducted to examine the influence of the values of A_m on the melting of a phase change material in thermal storage enclosures. Here, we consider the mushy zone constant A_m =

$1e5$ when dealing with iron and a mushy zone constant $A_m = 5e7$ for slag. The higher value assigned to slag owes to difficulties in achieving convergence with lower parameter values.

3.2.2. Sliding mesh

The rotary kiln turning motion has a sizeable influence on the melting time due both to the increased heat transfer towards the bottom of the furnace bed and due to the enhanced mixing of the molten materials, which are dragged along with the wall. To account for this effect, the proposed model uses the sliding mesh technique in ANSYS Fluent [23]. The mesh of the subdomains Ω_B and Ω_R (see Fig. 9) is assumed to have a non-conformal interface on Σ. Since Ω_R represents the solid refractory wall comprising the drum, its mesh cell positions are updated at each time step through a rotation defined by a constant angular speed of $v_{rot} = \pi/40$ rad/s (0.75 rpm). This rotation also affects the cell faces lying on Σ, which are updated accordingly. The region Ω_B is not rotated. Instead, the drag experienced by the molten materials due to the kiln rotation is modelled by imposing a boundary condition, setting the appropriate fluid velocity.

3.2.3. Thermal buoyancy. Boussinesq model

As mentioned above, instead of considering a variable density, we maintain a constant density in the furnace load, as density changes with temperature are small. However, buoyancy due to thermal effects is significant, and is addressed using the Boussinesq model, which treats mass density as a constant value, and adds a source term to the right-hand side of the momentum conservation equation (3):

$$\mathbf{b} = -\rho_0 \beta \left(T - T_{ref,B}\right) \mathbf{g}$$

where ρ_0 is the (constant) mass density of the molten material, T denotes the temperature, $T_{ref,B}$ is the reference temperature for the Boussinesq model and β is the thermal expansion coefficient (see Table 2). Lastly, $\mathbf{g} = (0, -9.81)^T$ m/s^2 is the gravitational acceleration vector.

3.2.4. Model equations

The mathematical model for this problem includes similar conservation equations as the model for the gas combustion problem, excluding the equations for the conservation of the species, which are not involved in this problem. Also, the region occupied by the furnace load, Ω_B, is assumed to be opaque to radiation, and the radiation model described in 3.1.3 is not considered, since the radiation contribution due to the flame is implicitly accounted for with the temperature profile T_D imposed as a boundary condition, discussed below.

Specifically, the mass conservation equation (2) and momentum conservation equation (3) are solved in Ω_B, considering the material properties for iron or slag. Moreover, the energy conservation equation (7) is solved in Ω_B, neglecting the term due to species diffusion, and considering the enthalpy definition (17) including the latent heat, required by the melting model. In Ω_R, the heat equation (10) is solved.

Since the liquid iron viscosity is low, turbulence induced by both buoyancy and the furnace rotation is significant in the flow. Consequently, the RKE turbulence model is used, including Eqs. (4) and (5). However, when simulating the melting of slag, where the viscosity is substantially higher, the flow regime becomes to laminar. As a result, turbulence modelling is omitted, and the corresponding terms in Eqs. (2), (3) and (9) are neglected, e.g., those related to the eddy viscosity μ_T or the turbulent kinetic energy K.

3.2.5. Boundary and initial conditions

The boundary of Ω is decomposed as depicted in Fig. 9. On the external boundary, denoted as Γ_R^e, the same boundary condition (15) discussed in the gas combustion problem is set, which models the convection heat transfer with the air surrounding the furnace. Moreover, on Γ_R^i, which is the internal wall of the refractory, in contact with the hot gas within the rotary kiln, we impose a Dirichlet boundary condition that depends on time, i.e.:

$$T(\mathbf{x}, t) = T_D(t), \tag{19}$$

where the temperature profile T_D is obtained by fitting the average temperature on $\widehat{\Sigma}$ (see Fig. 7), computed after solving the gas combustion problem.

On Σ, which corresponds to the interface between the solid refractory and the slag or iron within the furnace, continuity of heat flux and temperature is imposed. Moreover, to account for the influence of the furnace rotation in the mixing of molten slag or iron, the velocity $\mathbf{v}$ is set to match to the rotation speed. On the boundary Γ_B^i, which corresponds to the surface of the furnace load, the temperature is set using the same Dirichlet condition as in (19). It is also assumed as a free-slip wall, setting that the velocity satisfies $\mathbf{v} \cdot \mathbf{n} = 0$.

As the initial condition, we set that the velocity is $\mathbf{v} = 0$ m/s. The turbulent variables are set as $K = 0$ m^2/s^2 and $\epsilon = 1$ m^2/s^3. Lastly, for the temperature, since the usual procedure in plant involves the preheating of the furnace for one hour, an initial temperature field is computed by solving the heat equation in the refractory Ω_R considering the previously described boundary conditions on Γ_R^i and Γ_R^e. In this case, since the kiln is empty, the computational domain is $\Omega = \Omega_R$, and the boundary Γ_R^i corresponds to the whole inner boundary of the annulus in Fig. 9. After solving this preliminary problem, a temperature field is obtained for the boundary condition in Ω_R. In the load, the initial temperature is set to 293.15 K.

4. Numerical results

The proposed model is solved using the commercial software ANSYS Fluent 22.2 [23]. It employs a cell-centred finite volume method for discretizing the conservation equations. The coupling of velocity and pressure is achieved through the SIMPLE iterative algorithm. Least Squares Cell-Based schemes are considered to handle the diffusive terms, while Second-Order Upwind schemes are utilized for the treatment of convective terms. Pressure interpolation is carried out using the PRESTO! scheme. Time discretization is done using a Second Order Implicit scheme. For a more in-depth understanding of these numerical schemes, interested readers are encouraged to refer to [23,30] for additional details.

4.1. Gas combustion problem

The model proposed in Section 3.1 is solved considering an end time $t_{end} = 5$ h with the main objective of finding the temperature profile on the internal wall of the kiln. Since small time steps are required at the beginning of the simulation, a starting time step $\Delta t = 1e{-}4$ s is selected and is gradually increased until reaching a value of $\Delta t = 0.1$ s.

To determine if the mesh size is adequate for a sufficiently accurate prediction of the temperature profile, the model is solved until reaching the time value $t = 1000$ s for different grid sizes. Specifically, the different meshes gathered in Table 3 are considered, where the number of cells, as well as the maximum skewness and minimum orthogonal quality of each mesh, are reported. Note that, with the definition in the software used for the solution of the computational model, the best possible skewness and orthogonal quality are 0 and 1, respectively (see [23]). In Fig. 10, Mesh 3 is depicted. The mesh is refined near the fuel and oxygen inlets to ensure an adequate characterization of the fluid dynamics. Furthermore, appropriate grid refinement is carried out near the interface separating the air and the refractory, $\widehat{\Sigma}$, to accurately determine the wall temperature.

In Fig. 11(a), the average temperature on $\widehat{\Sigma}$ over time is depicted. Moreover, in Fig. 11(b), the temperature along $\widehat{\Sigma}$ is shown with respect to the arc length of the curve. The findings indicate that Mesh 1 exhibits excessive coarseness, whereas the remaining meshes yield comparable

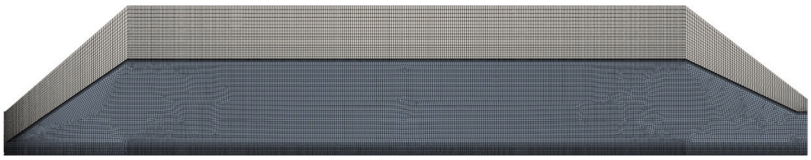

Fig. 10. Mesh 3 of the computational domain for the gas combustion problem.

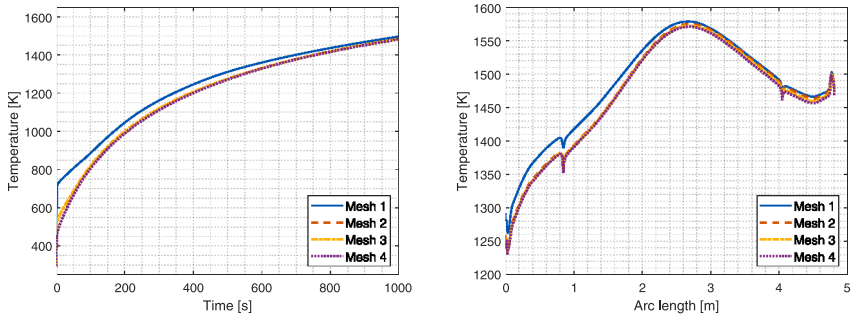

(a) Average temperature on $\widehat{\Sigma}$ over time. (b) Along $\widehat{\Sigma}$ at $t = 1000$ s.

Fig. 11. Temperature [K] for the different considered mesh sizes.

Table 3
Maximum skewness, minimum orthogonal quality and number of cells of the meshes considered for the gas combustion problem.

	Max. skewness	Min. orthogonal quality	Num. cells
Mesh 1	0.76	0.42	29 985
Mesh 2	0.76	0.50	54 047
Mesh 3	0.71	0.44	102 179
Mesh 4	0.72	0.43	208 843

Table 4
Maximum skewness, minimum orthogonal quality and number of cells of the meshes considered for the gas combustion problem.

	Max. skewness	Min. orthogonal quality	Num. cells
Mesh 1	0.86	0.15	1 223
Mesh 2	0.77	0.30	4 158
Mesh 3	0.77	0.30	16 632
Mesh 4	0.77	0.30	66 528

temperature values both over time and along the interface $\widehat{\Sigma}$. Therefore, we conclude that Mesh 3 is sufficiently fine to accurately predict the temperature profile over time in the wall, which is the main goal of this model. In the subsequently presented results for the gas combustion problem, Mesh 3 is used.

In Fig. 12, the computed velocity magnitude, temperature and mass fraction of O_2 are shown at the end time of the simulation, $t = 5$ h. Larger velocities are found near the fuel and oxygen inlets, with the flow also slightly accelerating as it approaches the open side of the furnace (right side of the figure). The streamlines of the flow show a large recirculation developing next to the inner wall. The highest temperature values are predicted in the middle section of the kiln, and the mass fraction of O_2 evidences a complete combustion of the injected oxygen.

The average temperature on the inner wall $\widehat{\Sigma}$ is computed over time until reaching the end time value. The obtained time-dependent curve is shown in Fig. 13. We observe a rapid increase in temperature during the initial stages of methane combustion. However, the rate of temperature build-up significantly decreases after the initial simulation stages. Nevertheless, it continues to rise throughout the entire simulated time interval, indicating that a period of 5 h is insufficient to reach a steady-state temperature in the solid refractory wall.

To define the boundary condition, the computed temperature is fitted to the following function (also depicted in Fig. 13):

$$T_D(t) = \begin{cases} 293.15 + \frac{t}{100}(838.32 - 293.15), & t \in [0, 100], \\ 838.32 + \frac{t-100}{400}(1284.7 - 838.32) & t \in (100, 500], \\ 1284.7 + \frac{t-500}{500}(1478.1 - 1284.7) & t \in (500, 1000], \\ at^b + c, & t \in (1000, 18000], \end{cases}$$

with $a = -10453$, $b = -0.3639$, $c = 2324.6$, and the time units being seconds.

4.2. Iron melting

Concerning the solid melting problem, the model described in Section 3.2 is solved. First, as mentioned previously, we consider material property values corresponding to iron and attempt to reproduce the usual procedure in plant to validate the model. The time-dependent temperature profile $T_D(t)$, computed after solving the gas combustion problem, is used as a boundary condition.

To assess if the mesh size is adequate, as in the gas combustion problem, we solve the model for the different grid sizes reported in Table 4. Note that the size of the subdomain corresponding to the load occupying the furnace, Ω_B, depends on the amount of material within the furnace. For this sensitivity study, we assume that the furnace is loaded with 3000 kg of iron. The height of the domain is computed assuming the constant density value reported in Table 1 and taking into account the geometrical features of the rotary kiln. In Fig. 14, Mesh 3 is depicted. The meshes are slightly refined near the interface with the solid, the vicinity of the free surface, and the corners on the sides of the domain.

The model is solved until reaching an end time value $t_{end} = 1.5$ h. The temperature initial condition in the refractory, Ω_R, is computed as described in Section 3.2.5 separately for each mesh in Table 4. In Fig. 15(a), the average liquid fraction is depicted over time for the different mesh sizes. While the general features of the curves obtained for the different meshes are similar, Mesh 1 and Mesh 2 lead to longer melting times, whereas the remaining curves overlap each other. Similar remarks apply to Fig. 15(b), where the temperature is shown along a vertical line splitting Ω_B in two symmetric halves. Again, Mesh 1 and Mesh 2 exhibit large differences compared to Mesh 3 and Mesh 4, which yield essentially identical vertical temperature profiles. We therefore conclude that Mesh 3 is sufficiently fine to solve the problem accurately. Henceforth, for a load equivalent to 3000 kg

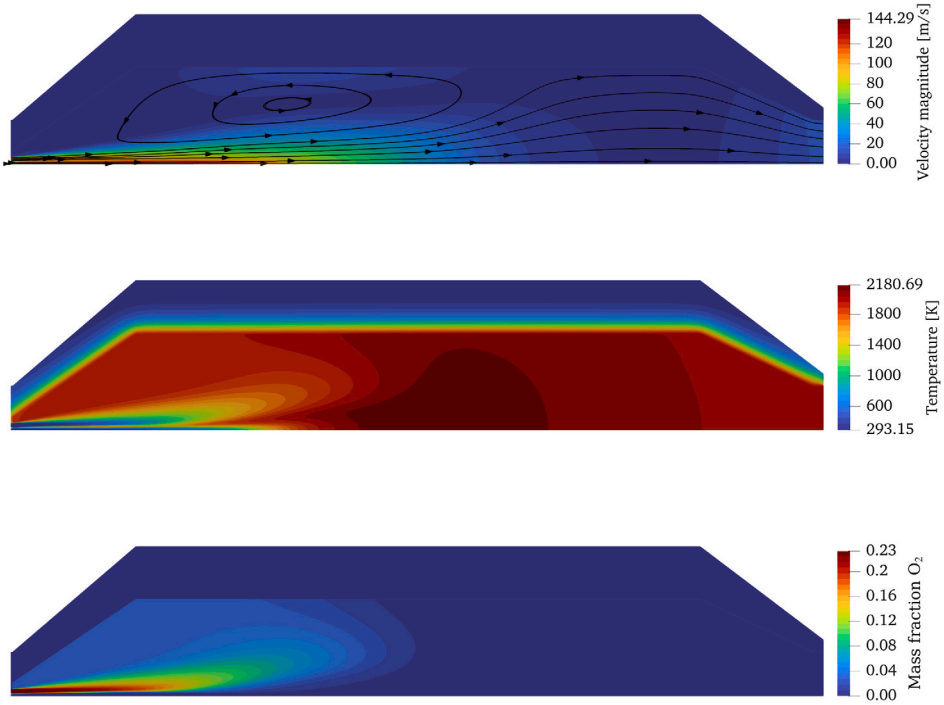

Fig. 12. Velocity magnitude [m/s] (top), temperature [K] (middle) and mass fraction of O_2 (bottom) in the gas combustion problem at $t = 5$ h.

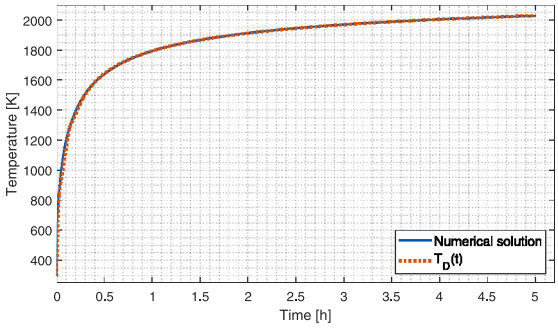

Fig. 13. Computed average temperature [K] on $\hat{\Sigma}$ over time and fitting function $T_D(t)$.

of iron, we employ Mesh 3 to obtain the numerical solution. For the scenarios involving different amounts of iron, the mesh will be adapted accordingly, maintaining a comparable element size to that used in this case.

Parametric study with respect to the iron mass

The solid melting problem is solved considering three different amounts of iron: 3000 kg, 3500 kg and 5000 kg. For each amount of iron, the height of the subdomain Ω_B is adjusted and the mesh is reconstructed appropriately. The iron load using during the standard plant procedure is typically around 3500 kg, with 5000 kg representing the maximum iron capacity of the furnace.

The temperature contours at times $t = 300$ s and $t = 1800$ s are shown in Fig. 16, for 3000 kg and 5000 kg of iron. The rotation of the furnace, which in the selected view of the domain is in the counter-clockwise direction (see Fig. 9), breaks the symmetry and leads to larger heat ingress in the bottom part of the furnace bed that is close to the corner on the left side. The solid core of iron remains at a lower temperature with larger mass values as time advances. The part of iron that remains in solid state is depicted in Fig. 17, where the liquid fraction contours for 3000 kg and 5000 kg are depicted for times $t = 300$ s and $t = 1800$ s. Only the subdomain corresponding to the furnace bed, Ω_B, is shown. Since the molten iron is dragged along with the wall motion, a larger molten zone develops on the left hand side. Also, due to the large range between the liquidus and solidus temperature of iron, there is a significant part of the kiln load at 1800 s that is above the solidus temperature but has not reached the liquidus temperature. Thus, a significant part of the furnace bed shows values of the liquid fraction that are strictly above zero and strictly below one, indicating the presence of a large mushy zone.

In Fig. 18, the velocity magnitude contours at the end time value $t = 1.5$ h are displayed for 3000 kg and 5000 kg of iron. Also, the streamlines of the flow are shown. At this time, the furnace bed is completely molten, as evidenced by the results shown in Fig. 17. The maximum velocity value in the scale has been adjusted to $1e{-}2$ m/s for clarity purposes, as the actual maximum value of the velocity, which is equal to the v_{rot} parameter ($4.32e - 2$ m/s), is only reached inside the boundary layer along the inner wall of the kiln. In addition to the primary circulation, which follows the motion of the wall, two large secondary eddies develop at the bottom of the load, more clearly observed in the case involving 5000 kg of iron.

As described in Section 2, the standard furnace procedure in plant involves three different casts after heating the empty furnace for 1 h. In the simulation of iron melting, to validate the model, we aim to reproduce this process numerically. Therefore, we simulate three consecutive casts. With this purpose, the mathematical model is solved starting with the initial condition described previously, at the end time corresponding to each of the subsequent casts in the plant, the values of the variables (temperature, velocity and the turbulence model variables) are reset to their initial values in the subdomain Ω_B. This resetting reflects the introduction of solid iron feed at ambient temperature into the hot furnace due to the previous casts, while maintaining the previously reached temperature in the refractory Ω_R.

In Fig. 19, the average liquid fraction over time is shown for the three casts. At the start of each cast the liquid fraction is zero in all Ω_B and rises until reaching one, point at which all the load is liquid. The trend followed by the curves resulting from all the considered cases is similar. As shown previously, the load melts significantly faster with less amount of iron. The specific time values required to reach complete

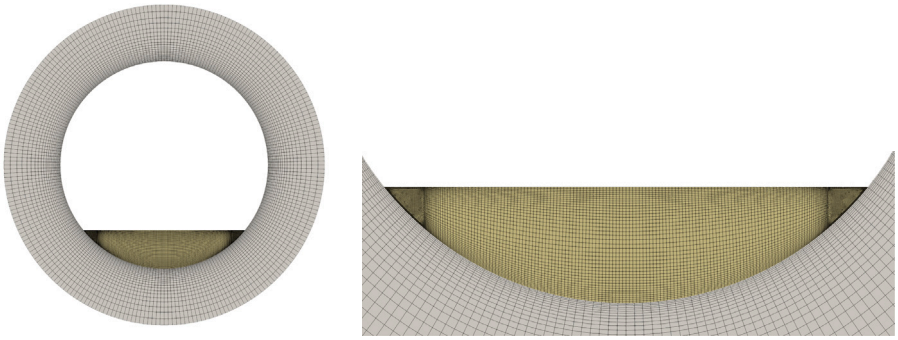

(a) Complete mesh. (b) Detail in the furnace bed.

Fig. 14. Mesh 3 of the computational domain for the melting problem.

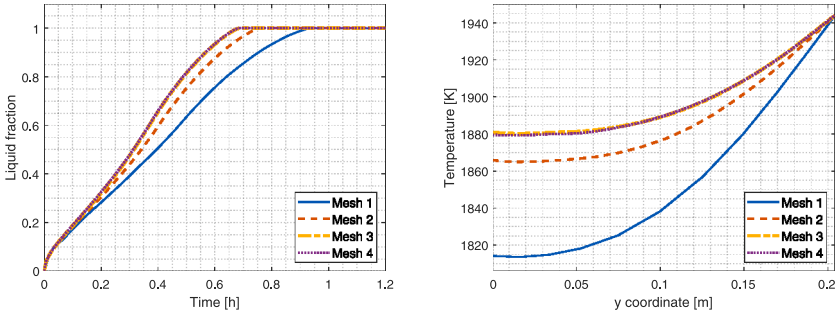

(a) Average liquid fraction over time. (b) Temperature on the vertical centreline at $t = 1.5$ h.

Fig. 15. Results for the different mesh sizes considered for the solid melting problem.

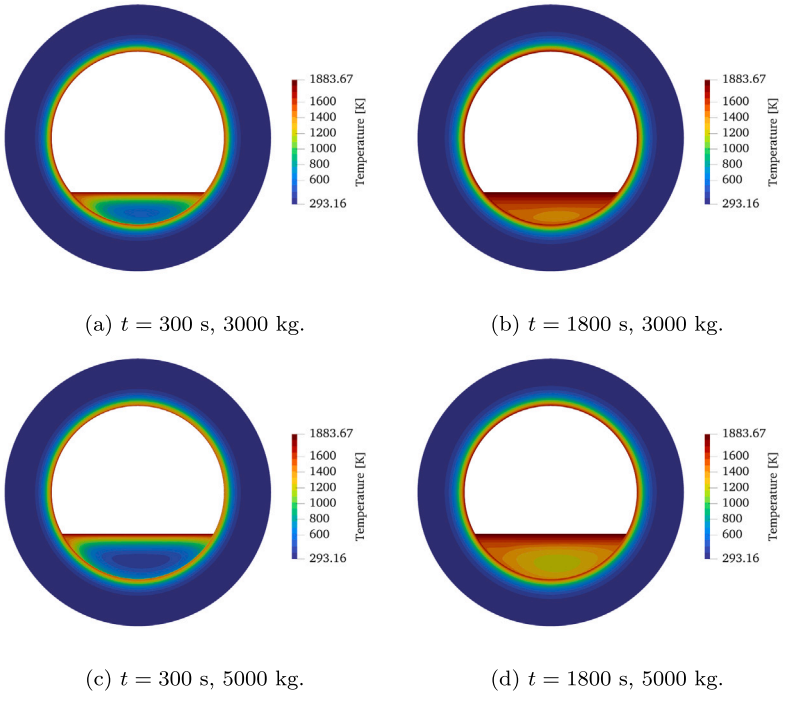

(a) $t = 300$ s, 3000 kg. (b) $t = 1800$ s, 3000 kg.

(c) $t = 300$ s, 5000 kg. (d) $t = 1800$ s, 5000 kg.

Fig. 16. Temperature [K] at different time values, considering 3000 kg and 5000 kg of iron.

melting are gathered in Table 5. The time values reported in the table have been normalized by subtracting the start time for each cast. It is observed that the first cast is slightly longer than the remaining ones for all amounts of iron, as the refractory is at a lower temperature.

Table 5 reports the relative reduction in time for each successive cast compared to the first, indicated in parentheses. Specifically, the third cast is approximately between 22% to 19% shorter than the first cast, with the difference being more pronounced when less iron

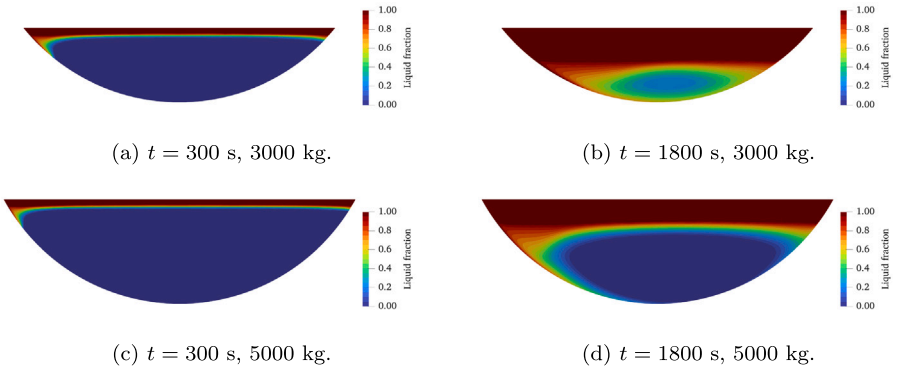

(a) $t = 300$ s, 3000 kg. (b) $t = 1800$ s, 3000 kg.

(c) $t = 300$ s, 5000 kg. (d) $t = 1800$ s, 5000 kg.

Fig. 17. Liquid fraction at different time values, considering 3000 kg and 5000 kg of iron.

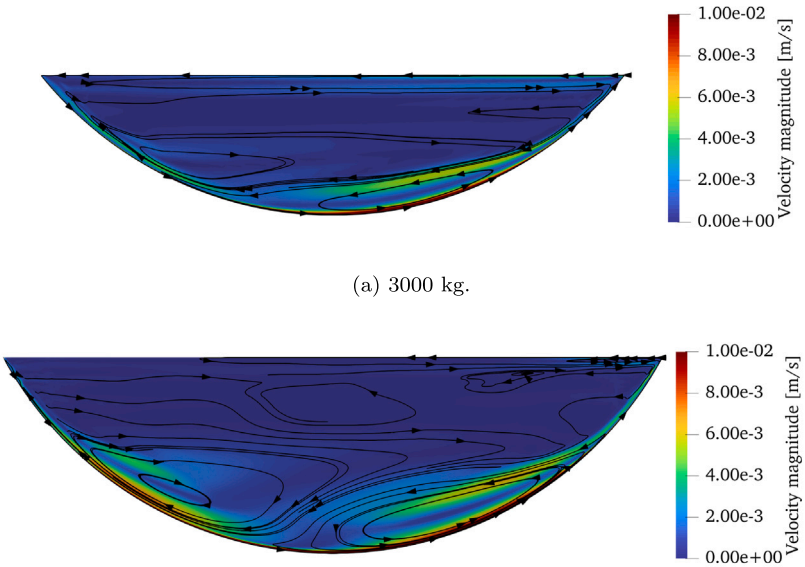

(a) 3000 kg.

(b) 5000 kg.

Fig. 18. Streamlines of the flow for different iron furnace loads at $t = 1.5$ h, coloured by velocity magnitude, considering 3000 kg and 5000 kg of iron.

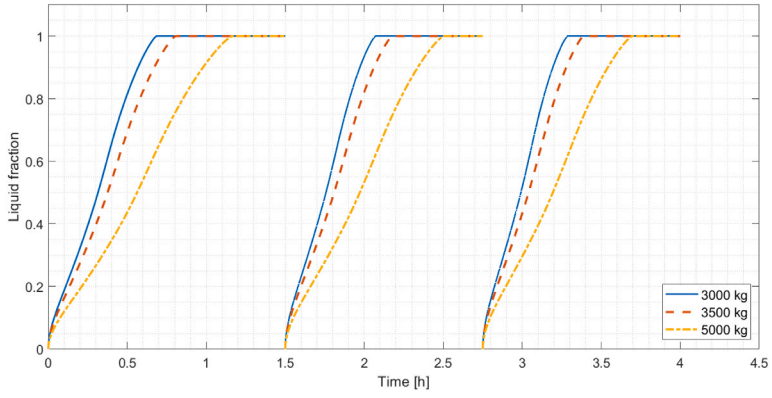

Fig. 19. Average liquid fraction over time for three casts for different values of iron mass.

is present. To illustrate this effect more clearly, Fig. 20 shows the average liquid fraction over normalized time values for both 3000 kg and 5000 kg of iron. Table 5 also indicates the average reduction in time as measured in the plant data, which closely matches the values obtained in our numerical simulations. Since the plant procedure involves varying conditions, typically with loads around 3500 kg, we calculate the average across different procedures. We do not provide the raw time data from the plant as it does not accurately reflect the actual time required to melt the load in the furnace. By the time the casting process is complete, the furnace charge may have been completely melted for a significant period of time, rendering the raw time data unreliable.

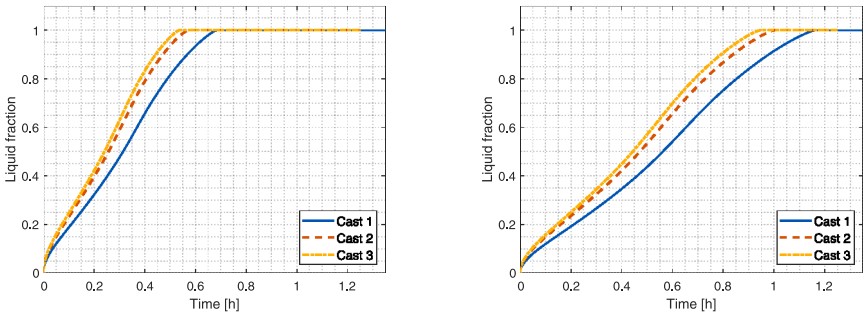

(a) 3000 kg. (b) 5000 kg.

Fig. 20. Comparison of the average liquid fraction over time during the different casts, for different iron amounts.

Table 5
Times (in hours) required to achieve complete melting for the different values of iron mass in three successive casts in the simulation. The values in parentheses indicate the relative reduction in time for the subsequent casts with respect to Cast 1, both in the simulation results and in the plant data.

	Simulation results			Plant data
	3000 kg	3500 kg	5000 kg	
Cast 1	0.69 (–)	0.81 (–)	1.17 (–)	(–)
Cast 2	0.57 (−17%)	0.68 (−16%)	1.00 (−15%)	(−22%)
Cast 3	0.54 (−22%)	0.64 (−21%)	0.95 (−19%)	(−26%)

If the time required to reach complete melting for different amounts of iron is compared, an approximate increase in time between 70% and 76% for stepping up from 3000 kg to 5000 kg is predicted by the model (see Table 5). This means that the furnace efficiency, measured in molten kg per minute, is slightly lower with 5000 kg if compared to that obtained with 3000 kg. For instance, during the first cast, 72.7 kg of iron are melted per minute with a 3000 kg load, as opposed to 71.4 kg of iron per minute considering a 5000 kg load.

Parametric study with respect to the rotation velocity

Considering 3000 kg of iron, the solid melting problem is solved varying the v_{rot} parameter. In addition to the previously considered kiln rotation speed of 0.75 rpm, we explore various rotation speeds ranging from 0 rpm to 1.5 rpm. Thus, the problem is solved adjusting the corresponding velocity v_{rot}, which is supplied as a boundary condition to the model.

Fig. 21(a) shows the average liquid fraction over time for the different rotation speeds. At higher rotation speeds, the intensified forced convection induced by faster furnace rotation results in accelerated melting times. Conversely, slower speeds result in significantly longer melting times. For instance, if the kiln does not rotate ($v_{rot} = 0$ rpm), the melting time exceeds 1.5 h, more than double the time taken at 0.75 rpm. These findings are summarized in Fig. 21(b), which shows the melting times as a function of the rotation speed in rpm. Within the range of 0.75 rpm to 1.5 rpm, we observed an essentially linear relationship between melting time and rotation speed, with a relative decrease in melting time of approximately 18% when doubling the rotation speed. It should be noted that, in the absence of furnace rotation, all liquid motion within the furnace bed is solely due to natural convection induced by buoyancy forces. On the other hand, since the iron is only heated from above, heat transfer is mainly by conduction and natural convection is not sufficient, which explains the slower melting times.

4.3. Slag melting

Under the same assumptions considered previously for iron, we investigate the viability of melting a CaO–SiO_2 slag suitable for the SisAl process. The furnace load material is replaced by slag, using the property values gathered in Section 2. The mathematical model is analogous, with the only exception that the flow is considered laminar, as discussed in Section 3.2. Since the slag is much less dense than iron, smaller amounts of slag can be loaded within the furnace. Thus, we solve the model considering a total load of 100 kg, 200 kg and 1000 kg.

In Fig. 22, the average liquid fraction is depicted over time for the different considered amounts of slag. As evidenced by the reported curves, the time values required to melt slag are much longer than those previously discussed for iron. In particular, for 200 kg of slag, more than 1.5 h are required to completely melt the load, as opposed to iron, where in the same interval the simulation predicted that 3000 kg could be melted. This is partly due to the slag low thermal conductivity, equal to 1 W/(m K) and roughly among 30 to 45 times less conducting than the iron that was considered in the previous results (see Table 1). Thus, the slag operates as an insulating material, significantly impeding the attainment of the melting temperature and slowing the melting process. Additionally, the latent heat of the slag is much larger than that of iron, implying that a larger amount of energy is required for the phase change. Lastly, the load is required to reach a temperature more than 150 K higher for the melting to complete when using slag.

In Figs. 23–25, the contours of the velocity magnitude with streamlines and liquid fraction are displayed at various time values for 100 kg, 200 kg and 1000 kg of slag, respectively. As opposed to the results previously shown for iron, the flow structures are notably simpler, characterized by a primary closed loop flowing in the direction induced by the turning motion. This behaviour is due to the higher viscosity of the slag, which results in the flow being predominantly governed by forced convection induced by the furnace rotation. At the corners of the furnace bed, for 200 kg and 1000 kg of slag, smaller loops are observed. The melting starts in these corners, as depicted in Fig. 25(b), and a high-temperature liquid layer quickly develops below the solid slag. This suggests that the turning motion is crucial for accelerating the melting process, as it allows to melt the slag from below.

The simulations of slag melting reveal the presence of a solid core within the furnace bed region over time. Since density changes with temperature are neglected, the model is unable to predict the gravitational settling of this solid core. However, considering the small density changes in the slag and the substantial viscosity of the molten slag, we speculate that the rotation of the furnace may effectively prevent the solid core from falling.

5. Conclusions

This article presents some of the work being carried out in the framework of the European project SisAl Pilot and, in particular, that related to a gas rotary kiln used for grey iron melting. A 2D transient mathematical model was devised and solved using a methodology comprising two distinct steps: firstly, a gas combustion problem was solved inside the kiln, including simulations of the natural gas flame and heat transfer by convection and radiation. From the solution of

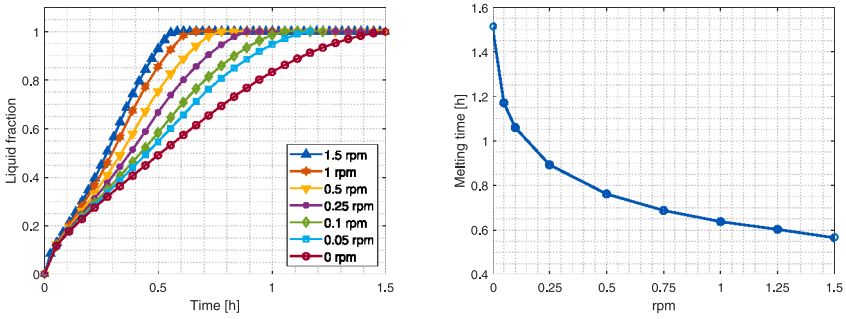

(a) Average liquid fraction over time. (b) Melting time against rpm.

Fig. 21. Sensitivity analysis of the melting time with respect to the furnace rotation parameter, v_{rot}.

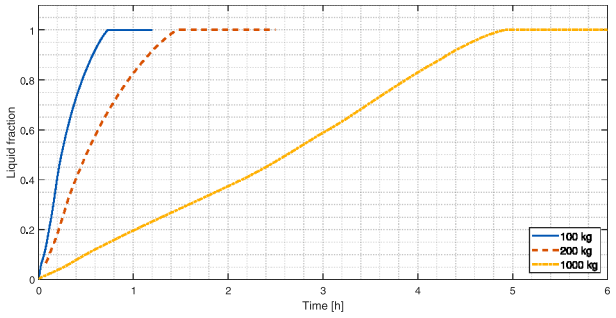

Fig. 22. Average liquid fraction over time for different amounts of slag.

this first problem, the temperature inside the furnace was obtained as a function of time. Subsequently, this data was used as boundary condition to determine the time required to melt the charge, taking into account both the rotation of the furnace and the natural convection in the molten liquid.

Validation of the mathematical model was conducted using iron as the furnace load, replicating the standard operating procedure of the facility, which involved preheating the furnace followed by three consecutive iron casts. The simulations demonstrated similar time reductions for subsequent casts relative to the first one, as observed in plant operations. The time required to melt the iron was found to be dependent on both the furnace speed and the amount of iron considered. In particular, doubling the speed from 0.75 to 1.5 rpm could reduce the melting time by about 18%, provided that a rotation speed of 1.5 rpm was structurally acceptable. Furthermore, scaling up iron mass from 3000 kg to 5000 kg resulted in a 70% to 76% increase in melting time, slightly reducing furnace efficiency in molten kg of iron per minute. Notably, the third cast was notably shorter (between 22% to 19%) than the first.

The feasibility of employing the furnace to melt a $CaO–SiO_2$ slag used in the aluminothermic reduction of quartz for silicon production was investigated. The numerical results revealed significantly longer melting times compared to iron due to its low thermal conductivity. For 200 kg of slag, more than 1.5 h are required to completely melt the load, as opposed to iron, where in the same interval the simulation predicted that 3000 kg could be melted. The rotational motion is crucial for accelerating the melting process of slag, as it allows to melt the slag from below.

Further work should be aimed at addressing some of the limitations of this study, namely, the modelling of natural gas as pure methane, neglecting gaps between solid material pieces, the assumption of a predetermined and constant shape of the furnace bed or the absence of volume expansion during melting. Although the analysis in this paper focuses on a particular type of rotary kiln, the presented model could be adapted to the study of other types of rotary furnaces, such as Top-Blown Rotary Converters (TBRC).

On the other hand, we have focused here on the main aspects of the research carried out in the SisAl Pilot project. However, the model developed could allow future research to be directed towards improving the performance and operation of this type of kiln, as well as analysing other possible parameters, such as the dimensions and refractory materials, potentially extending the applicability of the model.

CRediT authorship contribution statement

O. Crego: Software, Investigation, Conceptualization. **J.L. Ferrín:** Writing – review & editing, Writing – original draft, Visualization, Validation, Supervision, Software, Methodology, Investigation, Conceptualization. **D. Gómez:** Writing – review & editing, Writing – original draft, Visualization, Validation, Supervision, Software, Project administration, Methodology, Investigation, Funding acquisition, Conceptualization. **L.J. Pérez-Pérez:** Writing – review & editing, Writing – original draft, Visualization, Validation, Supervision, Software, Methodology, Investigation. **P. Salgado:** Writing – review & editing, Writing – original draft, Visualization, Validation, Supervision, Methodology, Investigation.

Declaration of competing interest

The authors declare that they have no known competing financial interests or personal relationships that could have appeared to influence the work reported in this paper.

Data availability

Data will be made available on request.

Acknowledgements

This work has received funding from the European Union's Horizon 2020 research and innovation program under Grant Agreement N° 869268. Also, it was partially supported by MCIN/AEI/ 10.13039/5011 00011033/FEDER, UE through grant PID2021-122625OB-I00 and by Xunta de Galicia funds under grant GRC GI-1563 - ED431C 2021/15.

The authors are particularly grateful to Fundiciones Rey, with special appreciation for Luis Rey and Susana Rey, and to Javier Bullón for providing the experimental data used in this work and for all the fruitful discussions.

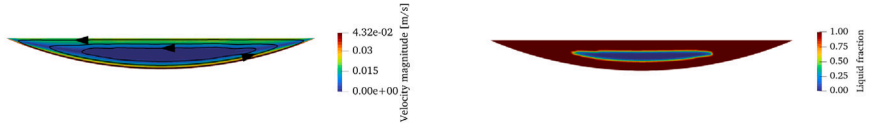

(a) Velocity magnitude, $t = 0.5$ h. (b) Liquid fraction, $t = 0.5$ h.

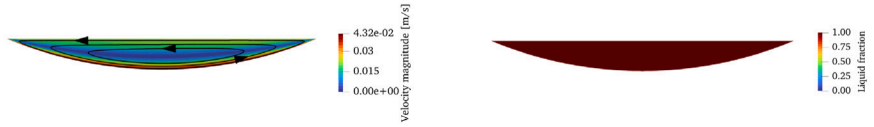

(c) Velocity magnitude, $t = 1$ h. (d) Liquid fraction, $t = 1$ h.

Fig. 23. Liquid fraction and velocity magnitude (with streamlines) for 100 kg of slag at different time values.

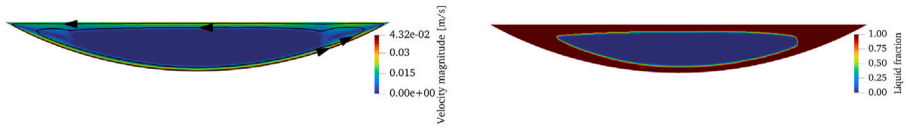

(a) Velocity magnitude, $t = 0.5$ h. (b) Liquid fraction, $t = 0.5$ h.

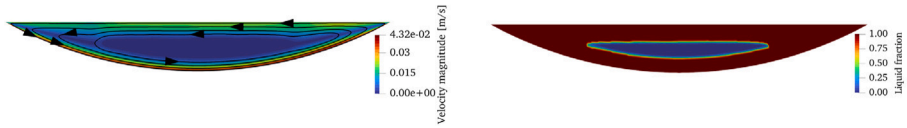

(c) Velocity magnitude, $t = 1$ h. (d) Liquid fraction, $t = 1$ h.

Fig. 24. Liquid fraction and velocity magnitude (with streamlines) for 200 kg of slag at different time values.

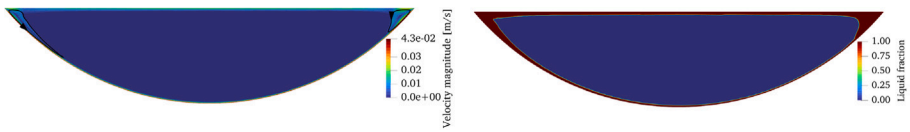

(a) Velocity magnitude, $t = 0.5$ h. (b) Liquid fraction, $t = 0.5$ h.

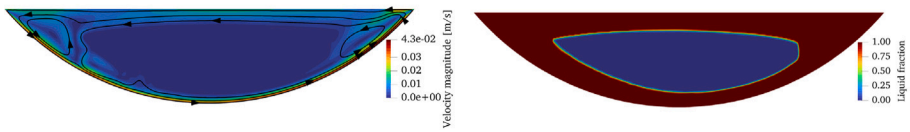

(c) Velocity magnitude, $t = 4$ h. (d) Liquid fraction, $t = 4$ h.

Fig. 25. Liquid fraction and velocity magnitude (with streamlines) for 1000 kg of slag at different time values.

References

[1] On the Review of the List of Critical Raw Materials for the EU and the Implementation of the Raw Materials Initiative, European Commission, 2014.

[2] J. Rumble, CRC Handbook of Chemistry and Physics, CRC Press, Boca Raton, FL, 2017.

[3] A. Ciftja, T.A. Engh, M. Tangstad, Refining and Recycling of Silicon: A Review, Norwegian University of Science and Technology, Trondheim, 2008.

[4] S.-H. Maeng, H. Lee, M.S. Park, S. Park, J. Jeong, S. Kim, Ultrafast carbothermal reduction of silica to silicon using a CO2 laser beam, Sci. Rep. 10 (1) (2020) 21730.

[5] H. Philipson, K. Blandhol, K. Engvoll, V. Djupvik, M. Wallin, G. Tranell, T. Haarberg, Preliminary techno-economic considerations of the sisal process - closing materials loops through industrial symbiosis, in: Proceedings of the Silicon for the Chemical & Solar Industry XVI, SSRN Journal, 2022.

[6] J. Bullon, New metallurgical way for the solar silicon production - the sisal project, in: Proceedings of the Silicon for the Chemical & Solar Industry XVI, SSRN Journal, 2022.

[7] A. Toli, G.M. Tsaousi, E. Balomenos, D. Panias, M. Heuer, H. Philipson, G. Tranell, Sustainable silicon and high purity alumina production from secondary silicon and aluminium raw materials through the innovative SisAl technology, Mater. Proc. 5 (1) (2021) 85.

[8] B.-J.R.M. Bisulandu, F. Huchet, Rotary kiln process: An overview of physical mechanisms, models and applications, Appl. Therm. Eng. (2022) 119637.

[9] M. Carmona, C. Cortés, Numerical simulation of a secondary aluminum melting furnace heated by a plasma torch, J. Mater Process. Technol. 214 (2) (2014) 334–346.

[10] E. Mastorakos, A. Massias, C. Tsakiroglou, D. Goussis, V. Burganos, A. Payatakes, CFD predictions for cement kilns including flame modelling, heat transfer and clinker chemistry, Appl. Math. Model. 23 (1) (1999) 55–76.

[11] K.S. Mujumdar, V.V. Ranade, CFD modeling of rotary cement kilns, Asia-Pac. J. Chem. Eng. 3 (2) (2008) 106–118.

[12] M. Wang, B. Liao, Y. Liu, S. Wang, S. Qing, A. Zhang, Numerical simulation of oxy-coal combustion in a rotary cement kiln, Appl. Therm. Eng. 103 (2016) 491–500.

[13] C. Pieper, S. Wirtz, S. Schaefer, V. Scherer, Numerical investigation of the impact of coating layers on RDF combustion and clinker properties in rotary cement kilns, Fuel 283 (2021) 118951.

[14] H.F. Elattar, E. Specht, A. Fouda, S. Rubaiee, A. Al-Zahrani, S.A. Nada, Swirled jet flame simulation and flow visualization inside rotary kiln-CFD with PDF approach, Processes 8 (2) (2020) 159.

[15] K. Mujumdar, V. Ranade, Simulation of rotary cement kilns using a one-dimensional model, Chem. Eng. Res. Des. 84 (3) (2006) 165–177.
[16] W. Rong, B. Li, Y. Feng, P. Schwarz, P. Witt, F. Qi, Numerical analysis of size-induced particle segregation in rotating drums based on Eulerian continuum approach, Powder Technol. 376 (2020) 80–92.
[17] P.J. Witt, J. Johnson, M.P. Schwarz, An efficient method for computational flow-based simulation of heat transfer in a rotary kiln with pilot scale validation, Appl. Therm. Eng. 214 (2022) 118894.
[18] B. Zhou, Y. Yang, M.A. Reuter, U.M. Boin, CFD-based process modelling of a rotary furnace for aluminium scrap melting, Prog. Comput. Fluid Dyn. Int. J. 7 (2–4) (2007) 195–208.
[19] G.K. Gaurav, S. Khanam, Computational fluid dynamics analysis of sponge iron rotary kiln, Case Stud. Therm. Eng. 9 (2017) 14–27.
[20] S.O. Alexopoulos, J. Dersch, M. Roeb, R. Pitz-Paal, Simulation model for the transient process behaviour of solar aluminium recycling in a rotary kiln, Appl. Therm. Eng. 78 (2015) 387–396.
[21] E. Alonso, A. Gallo, M. Roldán, C. Pérez-Rábago, E. Fuentealba, Use of rotary kilns for solar thermal applications: Review of developed studies and analysis of their potential, Sol. Energy 144 (2017) 90–104.
[22] Z. Ignaszak, P. Popielarski, J. Hajkowski, E. Codina, Methodology of comparative validation of selected foundry simulation codes, Arch. Foundry Eng. 15 (4) (2015) 37–44.
[23] Inc ANSYS, ANSYS® Fluent, Release 2022 R2 Theory Guide, ANSYS, Inc, 2022.
[24] D.C. Wilcox, Turbulence Modeling for CFD, DCW Industries, 2006.
[25] A.A. Gamil, T. Nikolaidis, I. Lelaj, P. Laskaridis, Assessment of numerical radiation models on the heat transfer of an aero-engine combustion chamber, Case Stud. Therm. Eng. 22 (2020) 100772.
[26] B.F. Magnussen, B.H. Hjertager, On mathematical modeling of turbulent combustion with special emphasis on soot formation and combustion, Symp. (Int.) Combust. 16 (1) (1977) 719–729.
[27] E. Vasquez, T. Eldredge, Process modeling for hydrocarbon fuel conversion, in: Advances in Clean Hydrocarbon Fuel Processing, Elsevier, 2011, pp. 509–545.
[28] M.F. Modest, Radiative Heat Transfer, Academic Press, 2013.
[29] T.F. Smith, Z.F. Shen, J.N. Friedman, Evaluation of coefficients for the weighted sum of gray gases model, J. Heat Transfer 104 (4) (1982) 602–608.
[30] H.K. Versteeg, W. Malalasekera, An Introduction to Computational Fluid Dynamics: The Finite Volume Method, Pearson Education, 2007.
[31] T.L. Bergman, T.L. Bergman, F.P. Incropera, D.P. Dewitt, A.S. Lavine, Fundamentals of Heat and Mass Transfer, John Wiley & Sons, 2011.
[32] V.R. Voller, C. Prakash, A fixed grid numerical modelling methodology for convection–diffusion mushy region phase-change problems, Int. J. Heat Mass Transfer 30 (8) (1987) 1709–1719.
[33] M. Fadl, P.C. Eames, Numerical investigation of the influence of mushy zone parameter A_{mush} on heat transfer characteristics in vertically and horizontally oriented thermal energy storage systems, Appl. Therm. Eng. 151 (2019) 90–99.